Performance Study of a Cantilevered Piezoelectric Energy Harvester

M.ENG. INDIVIDUAL RESEARCH PAPER

T. Bullock[1], A. Popov[2]

[1]Department of Mechanical, Materials and Manufacturing Engineering, University of Nottingham, United Kingdom
[2]Department of Mechanical, Materials and Manufacturing Engineering, University of Nottingham, United Kingdom

Author for correspondence: T. Bullock Email: efytb1@nottingham.ac.uk

Abstract

This project presents the modelling and simulation of a cantilevered piezoelectric energy harvester using both analytical and numerical methods. A MATLAB® model was developed based on the transfer matrix method (TMM) and Euler–Bernoulli beam theory, yielding a maximum output voltage of 0.9811 V at the resonant frequency. The model was validated against a 3D finite element simulation in COMSOL®, with results demonstrating excellent agreement in both resonant frequency (±1%) and voltage output (±2.6%). The study further investigated the effects of piezoelectric layer length and tip mass on device performance. Results highlight a strong dependence on resonant tuning and confirm the inherently narrow operating bandwidth typical of cantilevered piezoelectric harvesters.

Keywords: Piezoelectric Energy Harvesting, Transfer Matrix Method, COMSOL®, MATLAB®

1 Introduction

The increasing demand for portable, remote, low-power electronic devices such as wireless sensors [1–5] and wearable or implantable medical devices [6], has highlighted the limitations of their traditional power sources - batteries. Finite lifespan, highlighted in Figure 1, low power efficiency and limited energy storage capacity in addition to environmental impact make batteries an undesirable option [7]. Energy harvesting from ambient sources offers a promising alternative to power these devices sustainably. Among various ambient energy sources, such as those seen in Figure 2, mechanical vibrations are ubiquitous in both natural and man-made environments. Piezoelectric energy harvesting, which converts mechanical strain from vibrations into electrical energy, stands out due to its high power density, inherent electromechanical coupling, and efficiency at small scale [4].

Modelling and simulation of piezoelectric energy harvesters are crucial for understanding their performance, and addressing challenges such as operational bandwidth and transduction efficiency [8]. Despite advancements in materials, manufacturing techniques, and device architectures [9], opportunities remain to explore and quantify the key parameters that govern performance and contribute to energy losses in piezoelectric energy harvesters. The potential impact includes extending the operational life of low-power electronic devices, reducing reliance on batteries, enabling self-powered wireless sensor networks, and contributing to sustainable energy solutions.

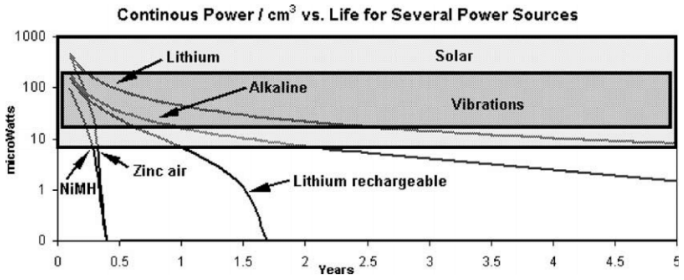

Figure 1: Comparison of power density over time for solar energy, vibration-based harvesting, and various battery technologies. Reproduced from [5].

1.1 Aim & Objectives

Aim

To study and understand piezoelectric energy harvesting devices through modelling and simulation techniques.

Objectives

1. To develop a MATLAB model of a piezoelectric energy harvesting device, using a cantilever beam model by work package 2.

2. To verify the MATLAB model by comparing it with results from FEA software, COMSOL, aiming for less than 10% discrepancy and validating with available experimental data. To be completed in work package

3.

3. To identify 3 primary performance parameters that affect the piezoelectric device's performance by the end of work package 4.

4. To conduct a sensitivity study on 3 key parameters that impact the performance of the piezoelectric device, quantifying their effects on output efficiency by the time the final report is due.

2 Literature Review

2.1 Energy Harvesting Techniques

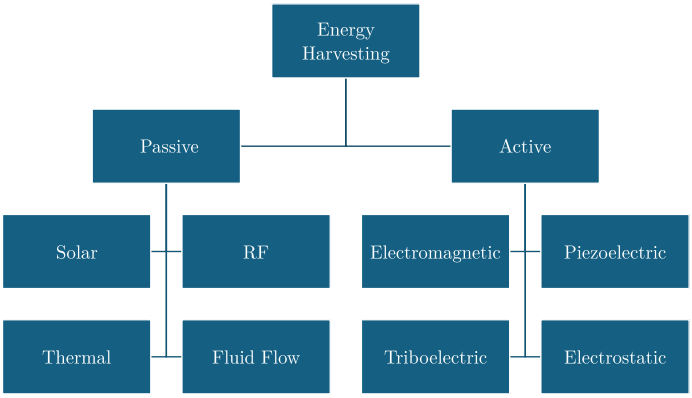

Figure 2: Taxonomy of energy harvesting sources.

The term energy harvesting is given to a process that captures and converts ambient energy from the environment into useful electrical energy [10, 11]. Figure 2 shows an overarching collection of the forms of energy harvesting, split into two main categories. Passive energy harvesting typically refers to capturing ambient energy from the environment at no cost, simply because it is already there. These are often the forms used in large scale renewable energy projects and generally produce megawatts of power [12]. Active energy harvesting refers to systems that are designed to capture/recycle otherwise wasted energy from human processes, such as kinetic energy in the form of vibrations. Due to the inherently small amplitude of vibrations, these devices are small by nature and typically generate power in the µW range [13]. Hereafter, these devices will be referred to as vibrational energy harvesters (VEHs), while acknowledging they are a subset of kinetic energy harvesters.

2.2 Piezoelectricity

The piezoelectric effect was first discovered by Jacques and Pierre Curie in 1880 [14]. When piezoelectric materials are subjected to mechanical strain, their molecular structure shifts, creating an electric polarisation that is proportional to the applied strain. This generates an electric charge on the surface of the material, which can then be collected as electrical energy and generate current through electrodes [11]. The piezoelectric effect functions in two distinct modes: direct and converse. In the direct effect, an applied mechanical strain induces an EMF. In the converse effect, the application of an EMF results in a mechanical strain, causing the material to deform. The direct effect is the mode used for piezoelectric VEHs.

2.3 Harvesting Methods & Applications

There are various configurations of piezoelectric energy harvesters proposed in the literature for a range of applications [2, 9, 15, 16]. A broad overview of various energy harvesting configurations will be provided, along with a justification for selecting a unimorph cantilever beam harvester for this project.

Cantilever beam based harvesters are the most common found in the literature, due to their simple structure and ease of manufacturing and modelling. In addition, they exhibit relatively low resonant frequencies and relatively high strain for a given force input, which is desirable for real world application [17]. They are often configured as either unimorphs, consisting of a single piezoelectric layer bonded to a substrate, or bimorphs, which feature two piezoelectric layers symmetrically bonded to either side of a substrate. Harvesters perform optimally when excited about their natural frequency, as this maximizes excitation, leading to maximum stress and voltage in the piezoelectric layer. Tuning the natural frequency to match the input frequency is commonly achieved by adding an inertial mass to the tip, as illustrated in Figure 3.

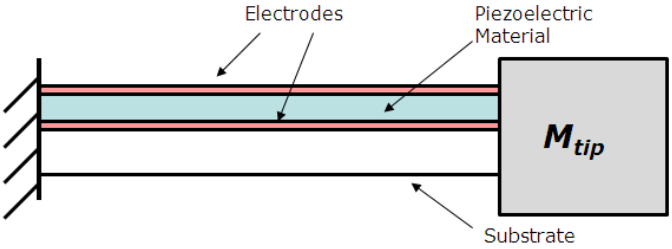

Figure 3: Unimorph cantilever beam configuration. Reproduced from [18].

There are various other form-factors reported in the literature which alter some form of the geometry in an attempt to increase performance. In some applications, it is not possible to fit a rigid piezoelectric structure. To address this issue, researchers have developed piezoelectric film that can be attached to oscillating bodies such as an aircraft [19]. Goldschmidtboeing *et al.* [20], experimented with triangle shaped beams and found that they outperform rectangular ones in terms of maximum output power. Interestingly, Rosa *et al.* [21], presented evidence suggesting the opposite, arguing that earlier studies had overlooked the impact of load resistance on electromechanical behaviour. Trapezoidal cross-section beams have also been modelled with different boundary conditions, such as clamped-clamped, with mixed success [17]. Karami *et al.* [22], proposed a zigzag structure which had a much lower natural frequency, ideal for ambient excitation as well as lower stress levels and therefore increased durability compared to cantilever

beams. This project will focus on developing a model for a unimorph cantilever beam, due to the time constraints on the project and the increased modelling complexity of other configurations.

2.4 Mathematical Modelling Techniques

The single degree of freedom (SDOF) model, initially proposed by William and Yates [23], was primarily developed for electromagnetic transduction. Researchers have used this approach to model piezoelectric VEHs [24, 25], however it has been shown to produce highly inaccurate results in such applications [26]. The SDOF model employs a 'lumped' approach, where the combined electromechanical damping is represented by a single equivalent damping coefficient. This oversimplification neglects critical physical phenomena, such as the distinct contributions of viscous air damping and strain-rate (Kelvin–Voigt) damping [27]. Furthermore, the SDOF approach fails to account for the contributions of higher vibration modes and overlooks spatial variations along the beam, such as the effects of the piezoelectric layer's position and distribution. These limitations highlight the need for more sophisticated modelling techniques.

Patel [18], models the unimorph structure using Euler-Bernoulli beam theory, which provides a distributed parameter model that captures spatial variations along the cantilever beam. Patel uses the transfer matrix method, TMM, to capture the mechanical behaviour in non-uniform structures, which allows for accurate modelling of the piezoelectric layer on the beam. The TMM, is a computational technique for analysing one dimensional mechanical systems by reducing complex problems to matrix operations. The system's state is output at selected cross-sections using state vectors and relates these via transfer matrices for each element. This modular methodology enables efficient computation of natural frequencies and mode shapes, forming a robust basis for analysing the behaviour. The approach will be particularly useful for sensitivity studies, as variables can be easily modified. This methodology will be adopted and utilised for this reason, as it will be pivotal in addressing objectives 3 and 4 of the project.

2.5 Limitations & Possible Solutions

A major challenge with the cantilever beam model is its narrow operating bandwidth. The efficiency decreases significantly when the device is not operating at or near its resonant frequency. This issue is further exacerbated by the fact that most applications for these devices require operation at low frequencies, which is contrary to the inherently high resonant frequencies of these beams. While the addition of a tip mass can help address this limitation, it introduces other challenges, such as increased bulkiness and risk of mechanical failure. Attempts to address this issue have been reported in the literature and can be classified into five mechanisms: multi degree of freedom harvesting (MDOF), mono-stable nonlinear harvesting, bi-stable nonlinear harvesting, frequency-up-conversion, and hybrid harvesting [6].

The MDOF approach expands the frequency range through two methods: multi-frequency and multi-directional. A multi-frequency harvesting system is designed to have multiple resonant frequencies, typically achieved by incorporating a series of spring-mass elements, thereby increasing the operating frequency range through multiple operating modes. A multi-directional harvesting system aims to scavenge vibrations in orthogonal directions. Chen *et al.* [28], arranged a number of piezoelectric cantilevers in a dandelion structure, so that they were sensitive to vibration from different directions. While promising, these approaches reduce the efficiency of device volume.

Mono-stable nonlinear harvesting involves intentionally introducing nonlinearity into the restoring force of the system, such as a preload into the structure or magnetic forces. The literature suggests that by introducing nonlinearity, the operational bandwidth can be increased [29]. Leland *et al.* [30], found that axially compressing a piezoelectric bimorph resulted in a 24% reduction in natural frequency along with increased coupling coefficients. Challa *et al.* [31], used a magnetic force technique to tune the frequency to $\pm 20\%$ of its untuned value.

Bi-stable nonlinear harvesting is similar to mono-stable except it has two steady state equilibrium points which when 'snapped' between enables significant energy extraction [6]. Frequency up conversion is the process by which low frequency ambient vibrations are converted into higher frequency oscillations, where piezoelectric energy harvesters are more efficient. This can occur through mechanical impact [32], mechanical plucking [33], snap through buckling [34] and magnetic plucking. Hybrid harvesting is the combination of multiple transduction mechanisms in one system. Combining transduction mechanisms, such as piezoelectric-electromagnetic, improves the power density efficiently and averages out the drawback on any single mechanism.

These solutions are promising in addressing the issue of narrow bandwidth. However, they significantly increase modelling complexity and due to time constraints are not within the scope of this project.

3 Methodology

The methodology of the project has been developed based off the findings from the literature review and in combination with the project requirements. The analytical model was implemented and simulated using MATLAB®, while the finite element model was developed in COMSOL®. Full derivations of the analytical formulation are not included in this report due to length constraints, but are comprehensively detailed by Patel [18].

3.1 Mechanical

The mechanical behaviour of the beam was modelled first, as the key outputs of this serve as inputs for determining the electrical behaviour.

3.1.1 Transfer Matrix Method

The mechanical behaviour will be modelled using a combination of Euler-Bernoulli and the transfer matrix method (TMM), as justified in Section 2.4.

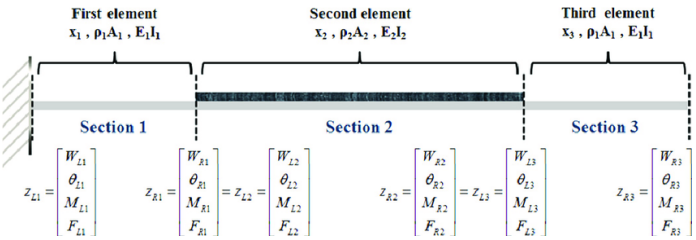

Figure 4: Piezoelectric Energy Harvester Model. Reproduced from [18].

The TMM assembles local transfer matrices for individual beam segments into a global transfer matrix, which can then be used to solve for the system's state variables at discrete points along its length and to determine the natural frequencies by applying appropriate boundary conditions. The modular nature of the TMM ensures that varying material properties, illustrated in Figure 4, are accounted for efficiently.

The state of the beam can be completely described by 4 variables: deflection (W), slope (θ), bending moment (M) and shear force (F), shown in Equation 1. The transfer matrix method for a beam assumes classical Euler-Bernoulli beam bending assumptions.

$$\mathbf{z_i}(x) = \begin{Bmatrix} W(x) \\ \theta(x) \\ M(x) \\ F(x) \end{Bmatrix} \tag{1}$$

The TMM initially begins with the Euler-Bernoulli beam equation:

$$\rho A \frac{\partial^2 W}{\partial t^2} + EI \frac{\partial^4 W}{\partial x^4} = F(x,t) \tag{2}$$

The derivation is omitted in this report, but the exact expression for the transverse motion of a beam of length i is given below, as derived from Equation 2:

$$W_i(x) = a \sin\left(\frac{\beta_i x}{l_i}\right) + b \cos\left(\frac{\beta_i x}{l_i}\right) + c \sinh\left(\frac{\beta_i x}{l_i}\right) + d \cosh\left(\frac{\beta_i x}{l_i}\right) \tag{3}$$

The constants a, b, c and d are determined from applying the boundary conditions. Here, x represents the position along the local beam element, and l_i denotes its length.

The term β_i is defined as:

$$\beta_i = \omega^{0.5} l_i \left(\frac{\rho_i A_i}{E_i I_i}\right)^{0.25} \tag{4}$$

Where I_i is the second moment of area, E_i is its Young's modulus, ρ_i is the material density, A_i is the cross-sectional area and ω is the excitation frequency.

In the case of the composite segment, i.e. an element composed of both the substrate and piezoelectric material the equivalent flexural rigidity becomes:

$$[EI]_{comp} = E_s I_{ys} + E_p I_{yp} \tag{5}$$

The parallel axis theorem was used to obtain the following:

$$I_{ys} = \frac{b_s {t_s}^3}{12} + b_s t_s \left(\bar{y} - \frac{t_s}{2}\right)^2 \tag{6}$$

$$I_{yp} = \frac{b_p {t_p}^3}{12} + b_p t_p \left(\frac{t_p}{2} + t_s - \bar{y}\right)^2 \tag{7}$$

The location of the neutral axis is defined by:

$$\bar{y} = \frac{t_s^2 b_s + t_p^2 n b_p + 2 t_s t_p n b_p}{2(t_s b_s + t_p n b_p)} \tag{8}$$

Where n is denoted as:

$$n = \frac{E_p}{E_s} \tag{9}$$

The terms b and t denote the width and thickness of each respective layer, and the subscripts $_p$ and $_s$ refer to the piezoelectric and substrate layers, respectively. This is illustrated clearly in Figure 5.

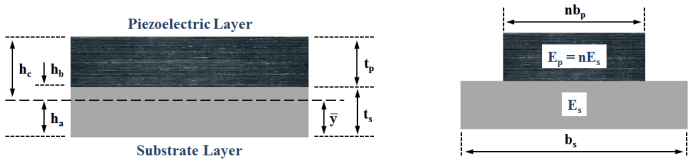

Figure 5: Unimorph energy harvester cross-section. Reproduced from [18].

Using the equations presented, the transfer matrix for a given element i was derived. In the TMM, the beam is discretised into n elements, one of which is illustrated in Figure 6, and the state variables at node i are determined from the state variables at the preceding node, $i-1$.

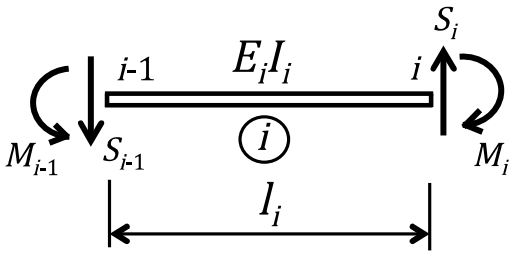

Figure 6: Beam element.

The derivation begins by employing classic beam bending relations:

$$\frac{\mathrm{d}F}{\mathrm{d}x} = q(x) \qquad \frac{\mathrm{d}M}{\mathrm{d}x} = S(x) \tag{10}$$

$$\frac{\mathrm{d}^2 W}{\mathrm{d}x^2} = \frac{\mathrm{d}\theta}{\mathrm{d}x} = \frac{M(x)}{EI} \qquad \frac{\mathrm{d}^3 W}{\mathrm{d}x^3} = \frac{F(x)}{EI} \tag{11}$$

For example, the shear force at either end of the element, shown in Figure 6, are related through the force equilibrium such that:

$$F_i = F_{i-1} \tag{12}$$

Therefore, this would constitute a 1 in the matrix.

The full derivation is omitted from this report for brevity; however, the process is repeated for each state variable, yielding the following transfer matrix for a piezoelectric cantilever beam:

$$\underbrace{\begin{Bmatrix} W_i \\ \theta_i \\ M_i \\ F_i \end{Bmatrix}}_{[\mathbf{z}]} = \mathbf{U}_i \underbrace{\begin{Bmatrix} W_{i+1} \\ \theta_{i+1} \\ M_{i+1} \\ F_{i+1} \end{Bmatrix}}_{[\mathbf{z_{+1}}]} \tag{13}$$

Where $\mathbf{U}_i$ is defined by:

$$\mathbf{U}_i = \begin{bmatrix} C_0 & -l_i C_1 & \frac{l_i^2 C_2}{E_i I_i} & \frac{l_i^3 C_3}{E_i I_i} \\ -\frac{\beta_i^4 C_3}{l_i} & C_0 & \frac{l_i C_1}{E_i I_i} & \frac{l_i^2 C_2}{E_i I_i} \\ -\frac{E_i I_i \beta_i^4 C_2}{l_i^2} & \frac{E_i I_i \beta_i^4 C_3}{l_i} & C_0 & l_i C_1 \\ -\frac{E_i I_i \beta_i^4 C_1}{l_i^3} & \frac{E_i I_i \beta_i^4 C_2}{l_i^2} & \frac{\beta_i^4 C_3}{l_i} & C_0 \end{bmatrix} \tag{14}$$

Constants C_0 to C_3 are defined by:

$$C_0 = \frac{\cosh(\beta_i) + \cos(\beta_i)}{2} \tag{15}$$

$$C_1 = \frac{\sinh(\beta_i) + \sin(\beta_i)}{2\beta_i} \tag{16}$$

$$C_2 = \frac{\cosh(\beta_i) - \cos(\beta_i)}{2{\beta_i}^2} \tag{17}$$

$$C_3 = \frac{\sinh(\beta_i) - \sin(\beta_i)}{2{\beta_i}^3} \tag{18}$$

As discussed in Section 2.5, the narrow operating bandwidth is a significant limitation of these devices. A tip mass is often introduced to tune the resonant frequency. This effect is incorporated into the TMM through the addition of a tip mass matrix, defined as:

$$\mathbf{U}_{\text{TIP}} = \begin{bmatrix} 1 & 0 & 0 & 0 \\ 0 & 1 & 0 & 0 \\ m_{\text{tip}}\omega^2 d & -(I_G + m_{\text{tip}}\omega^2 d^2) & 1 & 0 \\ -m_{\text{tip}}\omega^2 & m_{\text{tip}}\omega^2 d & 0 & 1 \end{bmatrix} \tag{19}$$

Where m_{tip} is the mass of the tip mass, I_G is its second moment of area, and d is the distance from the cantilever's free end to the tip mass centroid. In this project, the tip mass is modeled as a cuboid, leading to the following expressions:

$$m_{\text{tip}} = \rho_{\text{tip}} L_{\text{tip}} b_{\text{tip}} t_{\text{tip}} \tag{20}$$

$$I_G = \frac{b_{\text{tip}} {t_{\text{tip}}}^3}{12} \tag{21}$$

$$d = \frac{L_{\text{tip}}}{2} \tag{22}$$

The global transfer matrix is obtained by sequentially multiplying all individual transfer matrices, including the tip mass matrix, as follows:

$$\mathbf{U}_{\text{global}} = \mathbf{U}_{\text{TIP}} \mathbf{U}_n \mathbf{U}_{n-1} \cdots \mathbf{U}_2 \mathbf{U}_1 \tag{23}$$

3.1.2 Natural Frequency

To identify the natural frequencies, the beam is modelled under free vibration conditions. For a cantilever beam, the boundary conditions at the free end dictate that both the moment and shear force must be zero. As a result, the system's characteristic equation is formed by extracting the bottom right [2x2] submatrix of the global transfer matrix, corresponding to the moment and shear components, and setting its determinant to zero.

$$\det\left(\mathbf{U}_{\text{global}}(3{:}4,\ 3{:}4)\right) = 0 \tag{24}$$

This condition stems from the physical requirement that the free end of the beam must be able to vibrate without any applied force or constraint. By enforcing zero shear force and bending moment at the tip, the system is allowed to exhibit natural, undisturbed vibration modes that arise purely from its own structural dynamics. These modes only occur at specific frequencies (ω), which define the natural frequencies of the system. These frequencies were determined by finding the values of ω which satisfy the condition in Equation 24. Peak performance occurs at the fundamental frequency and therefore only the first mode is considered in this project [18].

The MATLAB® FZERO function was used to numerically find this value and enables efficient calculation when looping through other variables.

3.1.3 Mode Shape

Once the natural frequency of the beam was determined, the corresponding mode shapes were calculated. Using the natural frequency, the transfer matrix in Equation 14 could be constructed and the global transfer matrix was obtained using the relation in Equation 23. After this the following relation was obtained using the boundary conditions:

$$\underbrace{\begin{Bmatrix} 0 \\ 0 \\ M_i \\ F_i \end{Bmatrix}}_{[\mathbf{z_{clamped}}]} = \mathbf{U}_{\text{global}} \underbrace{\begin{Bmatrix} W_{i+1} \\ \theta_{i+1} \\ 0 \\ 0 \end{Bmatrix}}_{[\mathbf{z_{free}}]} \tag{25}$$

The two unknowns at the clamped end are solved by extracting the bottom right [2x2] submatrix of the global

transfer matrix, similar to the natural frequency:

$$\underset{[2x2]}{\mathbf{D}} = \mathbf{U}_{\text{global}}(3{:}4,\, 3{:}4) \tag{26}$$

To satisfy the free-end boundary conditions $M = 0$ and $F = 0$, a non-trivial initial state is found by computing the null space of $\mathbf{D}$:

$$\underset{[2x1]}{\mathbf{v}} = \text{null}(\mathbf{D}) \tag{27}$$

The null vector represents a valid non-trivial initial state that satisfies the boundary conditions, however since mode shapes can be arbitrarily scaled, the shear force at the clamped end is normalised to unity. The corresponding moment is then scaled proportionally using the components of the null vector:

$$\mathbf{z}_0 = \begin{bmatrix} 0 \\ 0 \\ \frac{v_1}{v_2} \\ 1 \end{bmatrix} \tag{28}$$

Where v_1 and v_2 are the first and second elements of the null vector $\mathbf{v}$, respectively.

The state vector at the clamped end, $\mathbf{z_0}$, is then propogated through beam using the unique transfer matrix for each element, $\mathbf{U_i}$, seen in Equation 13. This yields the full state vector along the beam, from which the displacement is extracted to form the unnormalised mode shape for the entire beam.

Once the mode shape is computed from the propagated state vector, it must be normalised before further analysis. Normalisation ensures that the mode shape has a consistent scale and can be meaningfully compared across different configurations. Since the amplitude of a mode shape is arbitrary, it is conventionally scaled such that the total modal mass equals unity. This is achieved by satisfying the orthonormality condition:

$$\int_0^L W_r(x)\, m(x)\, W_s(x)\, dx = \delta_{rs} \tag{29}$$

Here, $W_r(x)$ and $W_s(x)$ are the mode shapes corresponding to modes r and s, $m(x)$ is the mass per unit length, and δ_{rs} is the Kronecker delta, which equals 1 when $r = s$, and 0 otherwise.

In this project, only the first mode is considered. Therefore, the mode shape $W_1(x)$ is normalised by enforcing the condition:

$$\int_0^L {W_1}^2(x)\, m(x)\, dx = 1 \tag{30}$$

To achieve this, the normalisation constant is computed as:

$$A = \int_0^L {W_1}^2(x)\, m(x)\, dx \tag{31}$$

The normalised mode shape is then defined as:

$$W_{1\,\text{norm}}(x) = \frac{W_1(x)}{\sqrt{A}} \tag{32}$$

The normalised slope of the beam is then defined as:

$$W'_{1\,\text{norm}}(x) = \frac{W'_1(x)}{\sqrt{A}} \tag{33}$$

Substituting Equation 32 into Equation 30 confirms that the modal mass becomes unity. This condition is critical when the mode shape is used in electromechanical coupling expressions, as it ensures consistent and physically meaningful scaling.
This was achieved in MATLAB® by using the TRAPZ to numerically integrate.The normalised mode shape can be seen in Figure 9.

3.2 Electrical

3.2.1 Electromechanical Coupling

Following the computation of the natural frequency and normalised mode shape, the voltage output of the piezoelectric energy harvester was determined through a coupled electromechanical model [35]. The mechanical response of the beam under harmonic base excitation is translated into an electrical output by the direct piezoelectric effect. This is achieved by evaluating the electromechanical coupling between the mechanical strain in the piezoelectric layer and the electric field generated across its electrodes. This relationship is governed by the piezoelectric constitutive equations, which define the electromechanical coupling between mechanical stress and electric displacement, as shown in Equations 34 and 35.

$$\sigma_{11}^p = E_p \varepsilon_{11}^p - E_p d_{31}\, (E_{\text{field}})_3 \tag{34}$$

$$D_3 = E_p d_{31} \varepsilon_{11}^p + \varepsilon_{33}^S\, (E_{\text{field}})_3 \tag{35}$$

Here, σ_{11}^p represents the axial stress in the piezoelectric layer, and ε_{11}^p is the corresponding axial strain. The term E_3 denotes the electric field across the thickness of the PZT layer, while D_3 refers to the electric displacement. The constant d_{31} is the piezoelectric strain coefficient, which relates mechanical strain to electric field. ε_{33}^S is the permittivity of the piezoelectric material measured at constant strain, and E_p is the Young's modulus of the piezoelectric material.

By combining fundamental beam theory with the piezoelectric constitutive equations, it is shown that the internal moment expression includes an additional coupling term, $\epsilon V(t)$:

$$M(x,t) = E_s I_s \frac{\partial^2 W(x,t)}{\partial x^2} + E_p I_p \frac{\partial^2 W(x,t)}{\partial x^2} + \epsilon V(t) \tag{36}$$

Where ϵ is the electromechanical coupling term and $V(t)$ is the voltage. ϵ is defined as:

$$\epsilon = -\frac{E_p b_p d_{31}}{2 t_p} \left[{h_c}^2 - {h_b}^2 \right] \tag{37}$$

Here, h_c and h_b are illustrated diagrammatically in Figure 5 and are denoted as:

$$h_b = t_s - \bar{y} \tag{38}$$

$$h_c = t_p + t_s - \bar{y} \tag{39}$$

The following terms are defined for convenience and are used to construct the voltage response model:

$$R_1 = \epsilon \left[W_1'(x_1 + x_2) - W_1'(x_1) \right] \tag{40}$$

The term W_1' represents the derivative of the normalised mode shape (i.e. the slope of the beam). x_1 and x_2 refer to the start and end of the piezoelectric layer along the beam, respectively. For example, if the piezoelectric layer covers the length of the beam, $x_1 = 0$ and x_2 would equal the beam length.

The term Q_1 represents the mechanical forcing function resulting from base excitation:

$$Q_1 = -Y_0 \omega^2 \int_0^L m(x) W_1(x)\, dx \tag{41}$$

Q_1 is proportional to the acceleration amplitude Y_0 and the square of the excitation frequency ω, and involves an integral of the mass distribution $m(x)$ weighted by the mode shape $W_1(x)$ along the beam length L. This term captures how the distributed inertia of the system contributes to the generation of electrical energy under dynamic excitation.

The internal capacitance is defined as:

$$C_p = \frac{\varepsilon_{33}^S b_p x_2}{t_p} \tag{42}$$

It is derived from the geometry and dielectric properties of the PZT material, where ε_{33}^S is the permittivity at constant strain, b_p is the width, x_2 is the length, and t_p is the thickness of the piezoelectric layer. This parameter influences the electrical impedance of the device and therefore directly affects the voltage output.

Finally, ϕ_1 is defined as:

$$\phi_1 = -\frac{E_p d_{31} t_{pc} b_p}{C_p} \left[W_1'(x_1 + x_2) - W_1'(x_1) \right] \tag{43}$$

The coupling coefficient, ϕ_1, links mechanical deformation to electrical output. Where E_p is the Young's modulus of the piezoelectric material, d_{31} is the piezoelectric strain constant, b_p is the width of the piezoelectric layer, and t_{pc} is the distance between the neutral axis and the piezoelectric material centre, defined as:

$$t_{pc} = t_s + \frac{1}{2} t_p - \bar{y} \tag{44}$$

These expressions collectively define the input parameters to the coupled electromechanical voltage model and are used in predicting the harvester's performance across a range of excitation frequencies.

3.2.2 Voltage Response

The coupled voltage response assumes the base motion is harmonic, therefore the voltage generated is also harmonic and can be expressed as:

$$V(t) = V_0 e^{i\omega t} \tag{45}$$

Where V_0 is the peak voltage, ω is the excitation frequency and t is time.

The final voltage expression, derived from the mechanical equations of motion and the piezoelectric constitutive relations as presented by Patel [18], is given below:

$$V(t) = \left[\frac{\dfrac{Q_1 \phi_1 i\omega}{(\omega_1^2 - \omega^2) + (2\gamma_1 \omega_1 \omega) i}}{\dfrac{R_1 \phi_1 i\omega}{(\omega_1^2 - \omega^2) + (2\gamma_1 \omega_1 \omega) i} + \left(i\omega + \dfrac{1}{C_p R_{\text{load}}} \right)} \right] e^{i\omega t} \tag{46}$$

Here, ω_1 is the natural frequency of the system, as determined from the mechanical model, γ_1 is the damping ratio, and R_{load} is the external electrical load resistance. This expression captures the voltage response of the piezoelectric harvester under harmonic excitation and fully accounts for the coupled electromechanical dynamics of the system.

3.2.3 Tip Displacement

The beam displacement relative to the base is denoted as:

$$w_{\text{rel}}(x,t) = W_1(x) \left[\frac{Q_1 - R_1 V_0}{\left(\omega_1^2 - \omega^2\right) + (2\gamma_1 \omega_1 \omega)\,\mathrm{i}} \right] e^{i\omega t} \tag{47}$$

3.3 Assumptions

A number of key assumptions have been made in this derivation which are outlined below:

- The harvester is assumed to have a constant rectangular cross-section along its length.
- Perfect bonding is assumed between the piezoelectric and substrate layers.
- Electrode and adhesive layers are considered to have negligible thickness.
- A uniform electric field is assumed across the thickness of the piezoelectric layer.
- Proportional damping is applied across all harvester configurations.
- Linear elastic behaviour is assumed for both the substrate and piezoelectric materials, and geometric nonlinearities are neglected.

3.4 COMSOL

To validate the analytical model, a full three-dimensional finite element model of the unimorph piezoelectric energy harvester was developed using COMSOL®. The software was selected for its inherent multiphysics capabilities, making it particularly well-suited for simulating

Table 1: Summary of COMSOL® simulation settings.

Setting	Details
Study Type	Frequency Domain Study
Mesh Type	Tetrahedral, Coarse
Damping	Rayleigh
Excitation	Base acceleration, $a_0 = 0.5\,\mathrm{m\,s^{-2}}$
Solver Type	ARPACK

electromechanical coupling phenomena such as those observed in piezoelectric materials.

The piezoelectric energy harvester was modelled within the native model builder environment of COMSOL®, and the final geometry is shown in Figure 7.

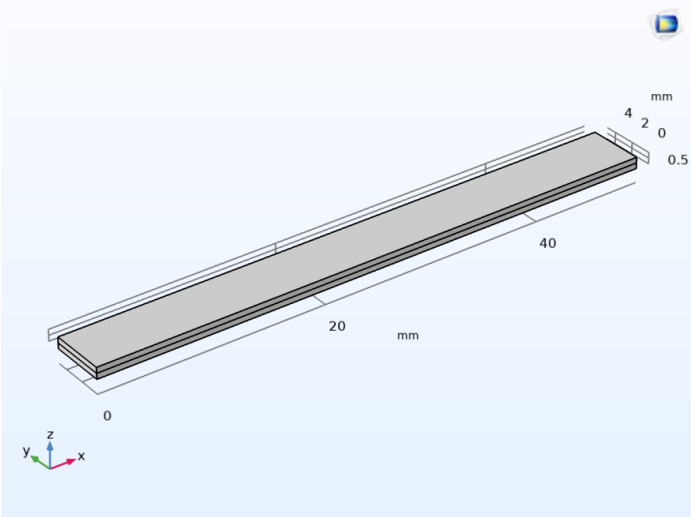

Figure 7: COMSOL® model of the piezoelectric energy harvester.

After constructing the geometry, material properties were assigned in accordance with the values listed in Tables 2 and 3.
A mesh convergence study determined that the optimal mesh setting was achieved using the 'coarse' mesh option. This was achieved by evaluating a range of mesh sizes and identifying the size at which the voltage output no longer changed significantly.
The electrostatic physics package was used to simulate the voltage response across the PZT layer, with a terminal and ground boundary condition applied at the top and bottom of the piezoelectric layer. The terminal and ground nodes were then connected through a lumped circuit interface that included the load resistor.

To equate the damping across both the COMSOL® and MATLAB® models, the following calculation was performed:

$$\gamma = \frac{\alpha}{2\omega} + \frac{\beta\omega}{2} \tag{48}$$

$$\alpha = 0 \tag{49}$$

$$\beta = \frac{0.01 \cdot 2}{1433.53} = 1.395 \times 10^{-5}\,\mathrm{s} \tag{50}$$

This approach neglects the mass-proportional damping term (α) and models damping solely through the stiffness-proportional term (β). At higher frequencies, the influence of α becomes less significant, as it primarily affects low-frequency behaviour. Therefore, setting $\alpha = 0$ provides a more accurate approximation of damping near the resonant frequency.
The model was then excited with a base acceleration of $a_0 = 0.5\,\mathrm{m\,s^{-2}}$, and the resulting voltage output across the piezoelectric layer was extracted and plotted as a function of excitation frequency.

4 Results

In the model analysed, it is assumed that the piezoelectric layer entirely covers the substrate and shares the same width and thickness. This configuration enables the energy harvester to be modelled as a single structural element with constant flexural rigidity and mass per unit length. The substrate is made of aluminium, while the piezoelectric layer is composed of PZT, the most widely used synthetic piezoelectric material. The geometrical and material properties of the beam are summarised in Table 2. Table 3 lists the electrical properties of PZT required for voltage calculations. A light mechanical damping factor ($\gamma = 0.01$) was applied. The beam geometry follows that used by Patel [18].

Table 2: Geometric and material properties of the piezoelectric harvester and tip mass. Reproduced from [18].

Parameter	Value
Substrate length [mm]	50
Substrate width [mm]	5
Substrate thickness [mm]	0.5
PZT length [mm]	50
PZT width [mm]	5
PZT thickness [mm]	0.5
Young's modulus of substrate [GPa]	69
Density of substrate [$\mathrm{kg\,m^{-3}}$]	2700
Young's modulus of PZT [GPa]	62.1
Density of PZT [$\mathrm{kg\,m^{-3}}$]	7800

Table 3: Piezoelectric material properties. Reproduced from [18].

Property	Value
Piezoelectric Constant (d_{31}) [$\mathrm{m\,V^{-1}}$]	-180×10^{-12}
Permittivity (ε_{33}^{S}) [$\mathrm{F\,m^{-1}}$]	1.549×10^{-8}

Figure 8 shows how the resonant frequency of the piezoelectric energy harvester changes with the length of the PZT layer. It is noted that at both ends, all configurations converge to the same result, as they represent identical beam configurations.
The 'clamped (PZT)' configuration exhibits a strong increase in resonant frequency with increasing PZT length,

Table 4: Tip mass geometry.

Parameter	Value
Length (l_{tip}) [mm]	5
Width (b_{tip}) [mm]	5
Thickness (t_{tip}) [mm]	5
Density (ρ_{tip}) [kg m^{-3}]	2700

reaching a peak of approximately 380 Hz at around 28 mm, before decreasing with a similar gradient. The 'free (PZT)' configuration shows an initial decrease in resonant frequency as PZT length increases, reaching a minimum of around 90 Hz at approximately 20 mm.
The tip mass configurations follow similar trends to their no-tip counterparts. The 'clamped (tip)' configuration shows a shallower increase in resonant frequency, reaching a maximum around 170 Hz at approximately 38 mm. The 'free (tip)' configuration displays a slight decrease, reaching a minimum of around 60 Hz at approximately 20 mm.

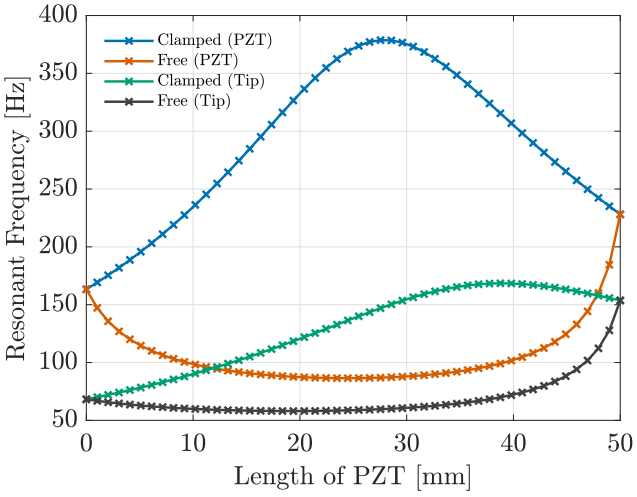

Figure 8: Resonant frequency of the harvester as a function of PZT layer length. The terms 'clamped' and 'free' indicate whether the PZT material is positioned at the clamped end or the free end of the beam, respectively. Each configuration includes the addition of a tip mass.

Figure 9 shows the normalised mode shape of the cantilever beam, plotted as normalised displacement against position along the beam length. The displacement increases smoothly from the clamped end ($x = 0$ m) to the free end ($x = 0.05$ m), where the maximum displacement occurs. The curve exhibits the typical nonlinear profile associated with the first bending mode of a cantilever beam, with displacement increasing more toward the free end. This can be verified with virtually all structural mechanics textbooks.

Figure 10 shows the voltage output of the piezoelectric energy harvester over a range of frequencies, using Equation 46.
In the open circuit condition, the voltage output exhibits

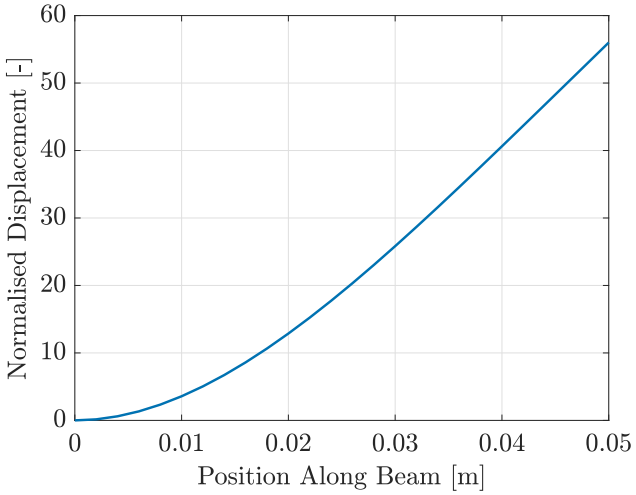

Figure 9: Normalised mode shape.

a sharp peak at the natural frequency ($\omega_n = 228$ Hz) of 0.9811 V. Away from resonance, the voltage drops of very quickly. Under closed circuit configuration produces negligible voltage output across the entire excitation frequency range.

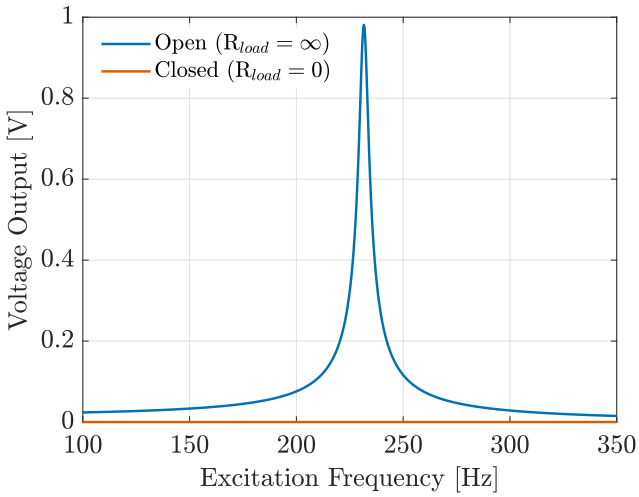

Figure 10: Voltage frequency response of the piezoelectric harvester in open and closed circuit configurations.

Figure 11 shows the tip displacement of the cantilever piezoelectric harvester as a function of excitation frequency.
The closed circuit case exhibits a maximum tip displacement of 0.0191 mm at a frequency of 228.1 Hz, while the open circuit case shows a slightly lower maximum displacement of 0.0188 mm occurring at 231.6 Hz. The open circuit condition results in both a reduced peak displacement and a shift in the natural frequency of the system; this phenomenon is explained in Section 5.

Figure 12 shows the voltage frequency response of the piezoelectric energy harvester as simulated using COMSOL® and MATLAB®. The general shape of both results is virtually identical, with the COMSOL® model exhibiting a slightly higher voltage output of 1.01 V compared to 0.9811 V of MATLAB®, a 2.6% difference. Addition-

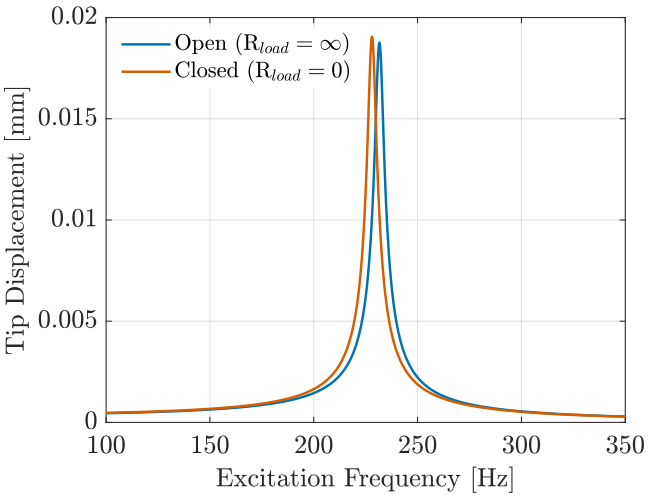

Figure 11: Tip displacement frequency response of the piezoelectric harvester in open and closed circuit configurations.

ally, the COMSOL® model has a slightly higher natural frequency of 234 Hz compared to 231.6 Hz of MATLAB®, a 1% difference.

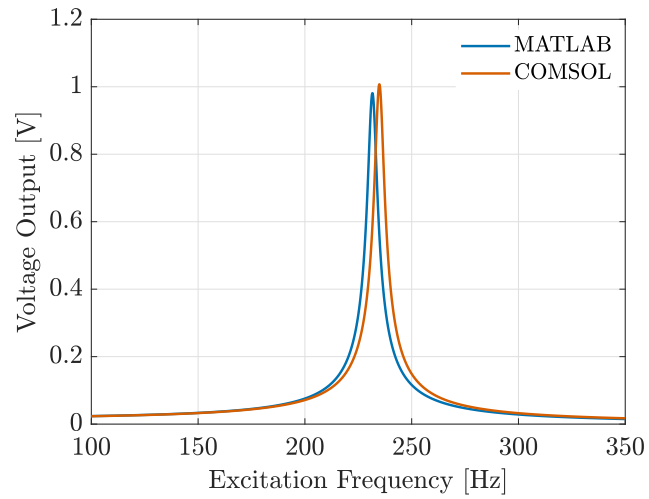

Figure 12: Voltage frequency response of the piezoelectric harvester: comparison between COMSOL® and MATLAB® simulations.

5 Discussion

The trends in Figure 8 can be explained by the interplay between stiffness and mass.
In the 'clamped' configuration, extending the PZT layer near the clamped end significantly stiffens the structure, making it more resistant to bending. This leads to an increase in resonant frequency, consistent with the relationship $f_n \propto \sqrt{\frac{k}{m}}$, where k is the stiffness of the system. However, as the PZT length continues to increase, the additional mass eventually outweighs the stiffness gain, resulting in a decrease in resonant frequency.
In the 'free' configuration, because the PZT is positioned at the free end, it primarily adds mass without significantly increasing stiffness. This causes a softening of the structure and a corresponding drop in resonant frequency.
For the tip mass configurations, the trends are similar but occur at lower frequencies. The presence of a tip mass increases the effective inertia without enhancing stiffness, thereby lowering the overall stiffness-to-mass ratio and reducing the natural frequency.
Finally, Figure 8 highlights the high degree of tunability inherent in these designs. By adjusting the PZT length and mass configuration, the resonant frequency can be matched relatively easily to a desired excitation frequency for specific real-world applications.

The observed mode shape in Figure 9 is typical of the first bending mode of a cantilever beam. At the clamped end, both displacement and slope are zero due to the boundary conditions, while at the free end, maximum displacement is observed. The curvature of the plot reflects the increasing flexibility along the beam's length, with larger deflections occurring further from the clamped boundary. This behaviour is consistent with classical Euler-Bernoulli beam theory.

The behaviour in Figure 10 is obviously due to the load resistance of the piezoelectric harvester. Under open circuit conditions, the generated charge has no path to dissipate, resulting in the accumulation of voltage and a sharp peak at the resonant frequency.
In the closed circuit case, the electrical load effectively short-circuits the piezoelectric element, allowing any generated charge to immediately dissipate, thus preventing any voltage buildup. Consequently, the harvester does not produce a voltage output under short-circuited conditions, regardless of the excitation frequency.
Figure 10 also clearly highlights the limited operating bandwidth of this type of device. This is evidenced by the fact that even an excitation frequency offset by just ±2% from the natural frequency results in the output voltage falling to half of its maximum value.

The similarity in the tip displacement profiles in Figure 11 for both electrical configurations indicates that the mechanical resonance is primarily governed by the structural properties of the beam. However, a slight difference in the resonant behaviour is observed and the closed circuit configuration exhibits a marginally higher peak displacement compared to the open circuit case. This is due to the influence of the electromechanical coupling of the piezoelectric material. Under open circuit conditions ($R_{load} = \infty$), the induced electrical charges cannot flow, resulting in an internal electric field that generates an opposing mechanical force. This 'back-coupling' increases the effective stiffness of the system, slightly raising the resonant frequency and reducing the peak displacement.
In contrast, under closed circuit conditions ($R_{load} = 0$), the generated charge is immediately dissipated, suppressing any internal electric field and nullifying the back-coupling effect. As a result, the system doesn't exhibit an electro-mechanical response purely a mechan-

ical one, hence why the natural frequency of the closed circuit is equal to that of the same configuration seen in Figure 8.
This behaviour is consistent with theoretical predictions, where the shift between open circuit and closed circuit resonant frequencies depends on the ratio of electromechanical coupling to mechanical damping, as captured by the expression [36]:

$$\omega_{oc} \approx \omega_1 \left(1 + \frac{R_1 \phi_1}{\omega_1^2 - 2\gamma_1^2}\right)^{1/2} \tag{51}$$

Where ω_{oc} is the open circuit resonant frequency and ϕ is the electromechanical coupling term defined in Equation 43. It is clear to see that stronger coupling leads to a more pronounced difference between the open and closed circuit resonant frequencies. For completion, $\omega_{oc} = 231.6\,\text{Hz}$, which aligns with the system in Figure 11.

The general agreement between the COMSOL® and MATLAB® results validate the analytical model implemented in MATLAB®. The minimal discrepancy in voltage magnitude is likely attributable to how the damping term was captured in Section 3.4. While setting $\alpha = 0$ provides the best available approximation, it is not exact. This likely resulted in a slight underestimation of the effective damping in the system, thereby producing a marginally higher voltage response. The slight overprediction of natural frequency in COMSOL® compared to the Euler–Bernoulli-based MATLAB® model can be attributed to COMSOLs® use of a full 3D elasticity formulation [37]. This inherently captures shear deformation, rotary inertia, and other cross-sectional effects, with the net effect of increasing the stiffness of the system. In contrast, the Euler–Bernoulli model neglects these effects, leading to a slightly lower predicted frequency. Nevertheless, the results are sufficiently close to be considered a successful validation of the analytical model.

5.1 Limitations

While the developed model provides a strong first approximation of energy harvester behaviour, several limitations arise from the simplifying assumptions made in Section 3.3. The assumptions of perfect bonding, uniform electric field distribution, and negligible adhesive thickness neglect real world inefficiencies that occur during manufacture and operation. Losses from these assumptions would lower the real performance compared to model predictions.
Additionally, the linear bending assumption restricts the model's accuracy to low amplitude vibrations, where strain remains proportional to applied force. At higher levels of base excitation, non-linear effects such as softening are known to occur, altering both the natural frequency and electrical output [18].

5.2 Future Work

One clear limitation that emerged from this project is the inherently narrow operating bandwidth of the cantilevered piezoelectric energy harvester. While the design is effective near resonance, its efficiency drops sharply outside this narrow frequency range. In future work, I would explore how different geometric configurations affect the operational bandwidth.
If repeating this project, I would also place greater emphasis on bandwidth expansion strategies earlier in the design process. Investigating the use of non-linear restoring forces, coupled MDOF systems, or passive frequency tuning mechanisms. These strategies can be found in the literature but were beyond the scope of this initial project.

6 Conclusion

This project set out to develop and validate a computational model for a cantilevered piezoelectric energy harvester. A comprehensive literature review was first conducted to establish the context and provide relevant background on current modelling techniques. A MATLAB® model was developed using the TMM and the methodology clearly outlined. The results obtained were identical with those reported by Patel [18], thereby validating the implementation. Subsequently, a full three-dimensional model was constructed in COMSOL®, and the output demonstrated strong correlation with the analytical results in both resonant frequency and voltage response. Several performance parameters were investigated as a function of excitation frequency. The influence of tip mass and piezoelectric coverage were all shown to significantly impact the resonant frequency of the device. These findings not only validate the implemented model but also provide insight into how such devices may be tuned for specific applications.
Overall, this work demonstrates the value of combining analytical and numerical methods for the study of piezoelectric harvesters. The methodology developed here provides a strong foundation for further optimisation and could be extended to support the design of more complex or application-specific devices.

7 Acknowledgments

Thanks to the University of Sydney for access to their COMSOL® licence.

References

[1] S. Roundy, P. K. Wright, and J. M. Rabaey, *Energy Scavenging for Wireless Sensor Networks: with Special Focus on Vibrations*, eng. Boston, MA: Springer US, 2004, ISBN: 1461504864.

[2] J. Lee and B. Choi, 'Development of a piezoelectric energy harvesting system for implementing wireless sensors on the tires,' *Energy Conversion and Management*, vol. 78, pp. 32–38, Feb. 2014, ISSN: 0196-8904. DOI: 10.1016/J.ENCONMAN.2013.09.054.

[3] Y. J. Yoon, W. T. Park, K. H. H. Li, Y. Q. Ng, and Y. Song, 'A study of piezoelectric harvesters for low-level vibrations in wireless sensor networks,' *International Journal of Precision Engineering and Manufacturing*, vol. 14, no. 7, pp. 1257–1262, Jul. 2013, ISSN: 20054602. DOI: 10.1007/S12541-013-0171-2.

[4] M. K. Stojčev, M. R. Kosanović, and L. R. Golubović, 'Power management and energy harvesting techniques for wireless sensor nodes,' *9th International Conference on Telecommunications in Modern Satellite, Cable, and Broadcasting Services, TELSIKS 2009 - Proceedings of Paper*, pp. 65–72, Dec. 2009. DOI: 10.1109/TELSKS.2009.5339410.

[5] S. Roundy, P. K. Wright, and J. Rabaey, 'A study of low level vibrations as a power source for wireless sensor nodes,' *Computer Communications*, vol. 26, no. 11, pp. 1131–1144, Jul. 2003, ISSN: 01403664. DOI: 10.1016/S0140-3664(02)00248-7.

[6] H. Liu, J. Zhong, C. Lee, S. W. Lee, and L. Lin, 'A comprehensive review on piezoelectric energy harvesting technology: Materials, mechanisms, and applications,' *Applied Physics Reviews*, vol. 5, no. 4, p. 041 306, Dec. 2018, ISSN: 19319401. DOI: 10.1063/1.5074184.

[7] J. L. Sullivan and L. Gaines, 'A review of battery life-cycle analysis : state of knowledge and critical needs.,' *U.S. Department of Energy Office of Scientific and Technical Information*, Dec. 2010. DOI: 10.2172/1000659.

[8] W. K. Seah, A. E. Zhi, and H. P. Tan, 'Wireless Sensor Networks Powered by Ambient Energy Harvesting (WSN-HEAP) - Survey and challenges,' *Proceedings of the 2009 1st International Conference on Wireless Communication, Vehicular Technology, Information Theory and Aerospace and Electronic Systems Technology, Wireless VITAE 2009*, pp. 1–5, 2009. DOI: 10.1109/WIRELESSVITAE.2009.5172411.

[9] M. Safaei, H. A. Sodano, and S. R. Anton, 'A review of energy harvesting using piezoelectric materials: State-of-the-art a decade later (2008-2018),' *Smart Materials and Structures*, vol. 28, no. 11, p. 113 001, Oct. 2019, ISSN: 1361665X. DOI: 10.1088/1361-665X/ab36e4.

[10] T. J. Kaźmierski and S. Beeby, *Energy Harvesting Systems: Principles, Modeling and Applications*, eng, 1. Aufl. New York, NY: Springer Science + Business Media, 2011, ISBN: 1441975659.

[11] S. Priya and D. J. Inman, *Energy harvesting technologies*, eng, S. Priya and D. J. Inman, Eds. New York ; London: Springer, 2009, ISBN: 0387764631.

[12] N. L. Panwar, S. C. Kaushik, and S. Kothari, 'Role of renewable energy sources in environmental protection: A review,' *Renewable and Sustainable Energy Reviews*, vol. 15, no. 3, pp. 1513–1524, Apr. 2011, ISSN: 1364-0321. DOI: 10.1016/J.RSER.2010.11.037.

[13] C. Wei and X. Jing, 'A comprehensive review on vibration energy harvesting: Modelling and realization,' *Renewable and Sustainable Energy Reviews*, vol. 74, pp. 1–18, Jan. 2017, ISSN: 18790690. DOI: 10.1016/j.rser.2017.01.073.

[14] S. P. Beeby, M. J. Tudor, and N. M. White, 'Energy harvesting vibration sources for microsystems applications,' *Measurement Science and Technology*, vol. 17, no. 12, R175–R195, Dec. 2006, ISSN: 13616501. DOI: 10.1088/0957-0233/17/12/R01.

[15] Z. Yang, S. Zhou, J. Zu, and D. Inman, 'High-Performance Piezoelectric Energy Harvesters and Their Applications,' *Joule*, vol. 2, no. 4, pp. 642–697, Apr. 2018, ISSN: 25424351. DOI: 10.1016/j.joule.2018.03.011.

[16] S. Chalasani and J. M. Conrad, 'A survey of energy harvesting sources for embedded systems,' *Conference Proceedings - IEEE SOUTHEASTCON*, pp. 442–447, 2008, ISSN: 1558058X. DOI: 10.1109/SECON.2008.4494336.

[17] S. Roundy *et al.*, 'Improving power output for vibration-based energy scavengers,' *IEEE Pervasive Computing*, vol. 4, no. 1, pp. 28–36, Mar. 2005, ISSN: 15361268. DOI: 10.1109/MPRV.2005.14.

[18] R. Patel, *Modelling analysis and optimisation of cantilever piezoelectric energy harvesters*, University of Nottingham. PhD Thesis. Engineering., Ed., 2013.

[19] U. Aridogan, I. Basdogan, and A. Erturk, 'Analytical modeling and experimental validation of a structurally integrated piezoelectric energy harvester on a thin plate,' *Smart Materials and Structures*, vol. 23, no. 4, p. 045 039, Mar. 2014, ISSN: 0964-1726. DOI: 10.1088/0964-1726/23/4/045039.

[20] F. Goldschmidtboeing and P. Woias, 'Characterization of different beam shapes for piezoelectric energy harvesting,' *Journal of Micromechanics and Microengineering*, vol. 18, no. 10, p. 104 013, Sep. 2008, ISSN: 0960-1317. DOI: 10.1088/0960-1317/18/10/104013.

[21] M. Rosa and C. De Marqui Junior, 'Modeling and Analysis of a Piezoelectric Energy Harvester with Varying Cross-Sectional Area,' *Shock and Vibration*, vol. 2014, 2014, ISSN: 10709622. DOI: 10.1155/2014/930503.

[22] M. A. Karami and D. J. Inman, 'Parametric study of zigzag microstructure for vibrational energy harvesting,' *Journal of Microelectromechanical Systems*, vol. 21, no. 1, pp. 145–160, Feb. 2012, ISSN: 10577157. DOI: 10.1109/JMEMS.2011.2171321.

[23] C. B. Williams and R. B. Yates, 'Analysis of a micro-electric generator for microsystems,' *Sensors and Actuators A: Physical*, vol. 52, no. 1-3, pp. 8–11, Mar. 1996, ISSN: 0924-4247. DOI: 10.1016/0924-4247(96)80118-X.

[24] H. B. Fang *et al.*, 'A MEMS-Based Piezoelectric Power Generator for Low FrequencyVibration Energy Harvesting,' *Chinese Physics Letters*, vol. 23, no. 3, p. 732, Mar. 2006, ISSN: 0256-307X. DOI: 10.1088/0256-307X/23/3/057.

[25] I. Jeon, M. Omiya, K. Kishimoto, T. Asahina, and S. Im, 'Modeling of a Gc-sensing element for the interfacial toughness of metal thin films on substrates,' *Sensors and Actuators A: Physical*, vol. 122, no. 2, pp. 291–300, Aug. 2005, ISSN: 0924-4247. DOI: 10.1016/J.SNA.2005.04.017.

[26] A. Erturk and D. J. Inman, 'Issues in mathematical modeling of piezoelectric energy harvesters,' *Smart Materials and Structures*, vol. 17, no. 6, p. 065 016, Dec. 2008, ISSN: 09641726. DOI: 10.1088/0964-1726/17/6/065016.

[27] A. Erturk and D. J. Inman, 'On Mechanical Modeling of Cantilevered Piezoelectric Vibration Energy Harvesters,' *http://dx.doi.org/10.1177/1045389X07085639*, vol. 19, no. 11, pp. 1311–1325, Apr. 2008, ISSN: 1045389X. DOI: 10.1177/1045389X07085639.

[28] R. Chen, L. Ren, H. Xia, X. Yuan, and X. Liu, 'Energy harvesting performance of a dandelion-like multi-directional piezoelectric vibration energy harvester,' *Sensors and Actuators A: Physical*, vol. 230, pp. 1–8, Jul. 2015, ISSN: 0924-4247. DOI: 10.1016/J.SNA.2015.03.038.

[29] B. P. Mann, 'Discussion: "On the role of nonlinearities in vibratory energy harvesting: A critical review and discussion" (Daqaq, M., Masana, R., Erturk, A., and Dane Quinn, D., 2014, ASME Appl. Mech. Rev., 66(4), p. 040801),' *Applied Mechanics Reviews*, vol. 66, no. 4, Jul. 2014, ISSN: 00036900. DOI: 10.1115/1.4027257.

[30] E. S. Leland and P. K. Wright, 'Resonance tuning of piezoelectric vibration energy scavenging generators using compressiveaxial preload,' *Smart Materials and Structures*, vol. 15, no. 5, p. 1413, Sep. 2006, ISSN: 0964-1726. DOI: 10.1088/0964-1726/15/5/030.

[31] V. R. Challa, M. G. Prasad, Y. Shi, and F. T. Fisher, 'A vibration energy harvesting device with bidirectional resonance frequency tunability,' *Smart Materials and Structures*, vol. 17, no. 1, p. 015 035, Jan. 2008, ISSN: 0964-1726. DOI: 10.1088/0964-1726/17/01/015035.

[32] M. Umeda, K. Nakamura, and S. Ueha, 'Analysis of the transformation of mechanical impact energy to electric energy using piezoelectric vibrator,' *Japanese Journal of*

Applied Physics, Part 1: Regular Papers and Short Notes and Review Papers, vol. 35, no. 5 B, pp. 3267–3273, May 1996, ISSN: 00214922. DOI: 10.1143/JJAP.35.3267.

[33] P. Janphuang, R. A. Lockhart, D. Isarakorn, S. Henein, D. Briand, and N. F. De Rooij, 'Harvesting energy from a rotating gear using an AFM-Like MEMS piezoelectric frequency up-converting energy harvester,' *Journal of Microelectromechanical Systems*, vol. 24, no. 3, pp. 742–754, Jun. 2015, ISSN: 10577157. DOI: 10.1109/JMEMS.2014.2349794.

[34] S. M. Jung and K. S. Yun, 'Energy-harvesting device with mechanical frequency-up conversion mechanism for increased power efficiency and wideband operation,' *Applied Physics Letters*, vol. 96, no. 11, Mar. 2010, ISSN: 00036951. DOI: 10.1063/1.3360219/338516.

[35] A. Erturk and D. J. Inman, 'A Distributed Parameter Electromechanical Model for Cantilevered Piezoelectric Energy Harvesters,' *Journal of Vibration and Acoustics*, vol. 130, no. 4, Jun. 2008, ISSN: 1048-9002. DOI: 10.1115/1.2890402. [Online]. Available: https://doi.org/10.1115/1.2890402.

[36] A. Erturk, *Piezoelectric Energy Harvesting*. eng, 1st ed., D. J. Inman, Ed. John Wiley & Sons, Incorporated, 2011, ISBN: 1119991161.

[37] Comsol, 'The Structural Mechanics Module User's Guide,' 2018. [Online]. Available: www.comsol.com/blogs.